# Response spectra for transient pore-pressure in a sandy seabed under random waves: Frequency-filtering effect[☆]

Jia-Hao Yu [a,b], Fu-Ping Gao [a,b,*], Chang-Fei Li [a,b]

[a] *Institute of Mechanics, Chinese Academy of Sciences, Beijing, 100190, China*
[b] *School of Engineering Science, University of Chinese Academy of Sciences, Beijing, 100049, China*

ARTICLE INFO

ABSTRACT

The real state of ocean waves is random in nature with various monochromatic components. Transient pore pressures in a sandy seabed under the action of the random-waves with JONSWAP spectrum and the regular-waves were physically modeled, respectively. The surface elevations and the corresponding transient pore pressures in the fine-sand were measured simultaneously in a wave flume. The frequency-filtering phenomenon was observed by Fourier analysis for random-wave induced pore pressure responses. In the Fourier energy spectra, both a primary-peak (high-frequency) and a secondary-peak (low-frequency) were identified within the relatively shallow soil layer. But the primary-peak kept declining rapidly, meanwhile the secondary-peak attenuated much more slowly with increasing soil depth, which can eventually lead to a shift between the high-frequency peak and the low-frequency one. As a consequence, the upgraded primary-peak frequencies of the dual-peaked spectra at the deeper soil layer would become smaller than the original significant frequencies, indicating that the pore pressure induced by long-wave components is of vital significance there. Furthermore, a filtering-depth parameter is introduced to characterize the frequency-filtering effect. Given the pore pressure at a certain soil depth, the quantitative relationship between the primary-peak and the secondary-peak can be predicted for an arbitrary soil depth.

## 1. Introduction

In offshore environments, wave-induced pore pressures in a porous seabed may weaken the soil strength, or even lead to soil liquefaction. As a consequence, the hazardous instability or failure of offshore structures could be triggered, e.g., the instability of breakwaters (see Jeng, 2001; de Groot et al., 2006; Ulker et al., 2010), the sinking/floatation of submarine pipelines (see Sumer et al., 1999; Miyamoto et al., 2020; Qi et al., 2020) and the collapse or instability of pile foundations (see Li et al., 2011; Gao et al., 2015; Sui et al., 2019).

Since the mid-twentieth century, a substantial amount of experimental, theoretical and numerical analyses have been conducted on the pore-pressure responses in a seabed under ocean waves (see the literature reviews by Jeng (2013)). On the basis of Biot's consolidation theory (Biot, 1941, 1955), Yamamoto et al. (1978) derived an analytical solution for regular-wave induced pore pressures in an isotropic seabed with infinite thickness, taking account of both the quasi-static deformation of the soil-skeleton and the compressibility of pore-fluid. Madsen (1978) established a general analytical method for solving Biot's consolidation equations to predict the transient pore pressures in an anisotropic seabed. Hsu and Jeng (1994) later extended the analytical solution to the seabed with finite thickness, which can converge to the solution of Yamamoto et al. (1978) as the soil depth approaches infinity. Recently, Li and Gao (2022) investigated the spatio-temporal distributions of pore pressures in a non-cohesive seabed and derived the relationship between the amplitude-attenuation and the phase-lag. It can be noticed that the previous studies on wave-induced pore pressures are predominantly limited to regular-wave conditions.

The real state of ocean waves is random in nature with various monochromatic components. Random-waves are commonly formed due to various influential factors from wind loading and seabed topography, etc. Longuet-Higgins (1975) investigated the joint distribution of the periods and amplitudes of sea waves. Several simplified statistical properties of random-waves were revealed subsequently. It was found that the apparent wave heights follow the Rayleigh distribution, and the initial phases follow the uniform distribution (Goda, 2000). The

---

[☆] This manuscript is the revised version submitted to ***Ocean Engineering*** for review.
[*] Corresponding author. Institute of Mechanics, Chinese Academy of Sciences, Beijing, 100190, China.
 *E-mail address:* fpgao@imech.ac.cn (F.-P. Gao).

distribution of wave frequencies has been commonly described with the Fourier energy spectra. And such an energy spectrum can be obtained by the Fourier transform of the signal's autocorrelation functions in the time domain, which is also known as the Wiener-Khintchine theorem (see Wiener,1930; Khintchine, 1934). The short-term propagation of random-waves is a steady stochastic process that satisfies stationarity and ergodicity (Stewart, 2006). The statistical characteristics of the random-waves can be epitomized by the significant wave heights and significant wave periods. Considering that actual ocean waves are three-dimensional, there are also directional spectra for random-waves to describe their internal directional structures. Generally speaking, two-dimensional wind wave spectra are concerned for both mathematical expediency and physical insight, among which the P-M and JONS-WAP spectra are the most typical and widespread ones.

The P-M spectrum was proposed to describe the fully-developed steady wind waves over a long period of time in a large ocean area (Pierson and Moskowitz, 1964). Nevertheless, Hasselmann et al. (1973) found that actual sea waves would never attain the fully-developed state when analyzing the data of JONSWAP (Joint North Sea Wave Project). Instead, waves would vary temporally, accompanied by nonlinear interactions between wave components during propagation. The JONS-WAP spectrum was thereby introduced. From then on, numerous reviews and investigations in terms of the JONSWAP spectrum were presented in the field of oceanography (see Hasselmann et al., 1980; Klopman and van der Meer, 1999; Kumar and Kumar, 2008; Goullet and Choi, 2011; Rueda-Bayona et al., 2020).

In the P-M spectrum (see Moskowitz, 1964), both a primary peak (corresponding to a higher frequency) and a secondary peak (to a relatively lower frequency) have been identified, which is attributed to the nonlinear interactions between spectral wave components (e.g., resonant excitations, white-capping, and swell). The wave energy can be gradually transferred from the short-wave to the long-wave components with relatively lower frequencies and energy densities, which tends to redistribute the energy more uniformly over the whole frequency domain (Hasselmann et al., 1973). Such a process might prompt a randomly generated long-wave noise (e.g., a weak infragravity wave bounded to a wave group, see Herbers et al., 1994) to grow progressively into a low-frequency peak, i.e., the secondary peak in the spectrum. Detailed discussions of the nonlinear effects can be found in Phillips (1960), Hasselmann (1962), Lake and Yuen (1978), and Ramamonjiar-isoa and Mollo-Christensen (1979). Since the pioneering work of Miles (1957, 1959) and Phillips (1957), how to formulate the generation and evolution of wind wave spectra appropriately has become a typical problem with a unified theoretical framework. Based on a modified unidirectional spatial version of the Zakharov equation, Shemer et al. (2020) established a numerical forecasting model of the evolution of young wind waves for a sufficient range of steady wind velocities. Liu et al. (2020) recently obtained the joint distributions of wave parameters and other marine parameters with the knowledge of statistics involved.

Besides the above-mentioned efforts on the inherent hydrodynamics of random-waves, the excess pore-pressure responses in a porous seabed under the action of random-waves have attracted much attention among researchers. Rahman and Layas (1986) examined random-wave induced soil responses associated with the pore-pressure buildup to evaluate the potential for the instability of a non-cohesive seabed under a storm condition. Sumer et al. (1999) measured the pore pressures in a silty bed under irregular-waves and deemed that the soil under irregular-waves could behave in a similar way as that under regular-waves. Liu and Jeng (2007) investigated the accurate expressions of two typical kinds of random-wave spectra (i.e., B-M and JONSWAP spectra) and acquired a semi-analytical solution for pore-pressure responses. Xu and Dong (2011) numerically studied the random-like waves with the Rayleigh distribution and performed a Monte-Carlo simulation of the pore-pressure responses. The existing semi-analytical and numerical results indicated that random-waves could induce much severer pore-pressure responses compared with the corresponding

regular-waves (see Liu and Jeng, 2007; Xu and Dong, 2011). Niu et al. (2019) utilized the wave breaking method to physically simulate secondary long-waves in a wave flume. It was recognized that the long-wave components of random-waves would contribute more significantly to the residual pore pressures in a silty seabed. It should be noted that the aforementioned efforts were mainly limited to time-domain analyses.

Quite a few physical phenomena in the natural environments (e.g., the heights of waves in a choppy sea, ground motion during an earthquake) have one thing in common, i.e., the unpredictability of their instantaneous values at any future time (Thomson and Dahleh, 2005; Booij et al., 1999; Ruiz and Saragoni, 2009; Diaz, 2016). The spectral analysis has been adopted for tackling random processes in the engineering practices. For the random-wave phenomenon, the energy spectra may provide a physical insight in the frequency domain, such as what the predominant components are, how often they take place and how they would interact with each other and evolve (Goda, 2000). The underlying mechanism for random-wave induced pore pressures in the frequency domain need to be further revealed.

In the present study, a series of flume tests were carried out to physically simulate the transient pore-pressure responses in a fine-sand bed under random-waves with JONSWAP spectra. The experimental results are compared with the existing analytical solution for regular-waves to distinguish the unique properties of pore-pressure responses under random-waves. Based on the flume measurements, Fourier analyses are made on the free water surface elevations and the pore pressures at various soil depths to obtain the corresponding response spectra of random-wave induced pore pressures. The group-bounded infragravity wave is speculated to appear in the frequency spectra as the secondary peak. The "frequency-filtering" phenomenon is observed and quantitatively analyzed by introducing the filtering-depth parameter. Furthermore, parametric analyses are implemented to explore the key influential factors for the frequency-filtering phenomenon.

## 2. Physical modeling

### 2.1. Experimental methodology

A series of experiments on both random-wave and regular-wave induced transient pore pressures in a sand bed were carried out in a large wave flume at the Institute of Mechanics, Chinese Academy of Sciences. As illustrated in Fig. 1(a), the major frame of the wave flume is 52.0 m in length, 1.0 m in width, and 1.5 m in height with transparent glass sidewalls. And a soil box (5.0 m in length, 1.0 m in width, and 0.6 m in depth) is located in the middle of the flume. The water depth ($d$) was kept as 0.6 m during the series of flume tests. A piston-type wave generator installed at the inlet of the flume could produce random-waves with various wave spectra. A beach-type wave absorber was constructed at the outlet of the wave flume to effectively avoid reflection of waves with the wave reflection coefficient less than 5% (see Fig. 1(a)). The generation of random-waves with a JONSWAP spectrum is detailed in Section 2.2.

A fine-sand bed was prepared in the soil box using the sand-raining method, which could effectively ensure that the sand bed is generally homogeneous and saturated (see Li and Gao, 2022). The particle size distribution of the fine-sand is shown in Fig. 2, and the main physical properties of the fine-sand are listed in Table 1. To measure the excess pore pressures, eleven miniature pore-pressure transducers (PPTs) were utilized at different depths within the sand bed (PPT-1 ~ PPT-11, at $z$ = 1 cm, 3 cm, 6 cm, 10 cm, 15 cm, 20 cm, 25 cm, 30 cm, 35 cm, 40 cm, and 50 cm, respectively, see Fig. 1(b)). The PPTs (1–11) were supported separately by the rigid brackets vertically fixed to the bottom of the flume (see Fig. 1(b)) to minimize their mutual interference within the soil. Another PPT (PPT-12, see Fig. 1(a)) was mounted at the surface of the bed to measure the wave pressure fluctuations at the mudline (i.e., $z$ = 0). Note: the probes of the PPTs are as tiny as 0.5 cm in diameter and
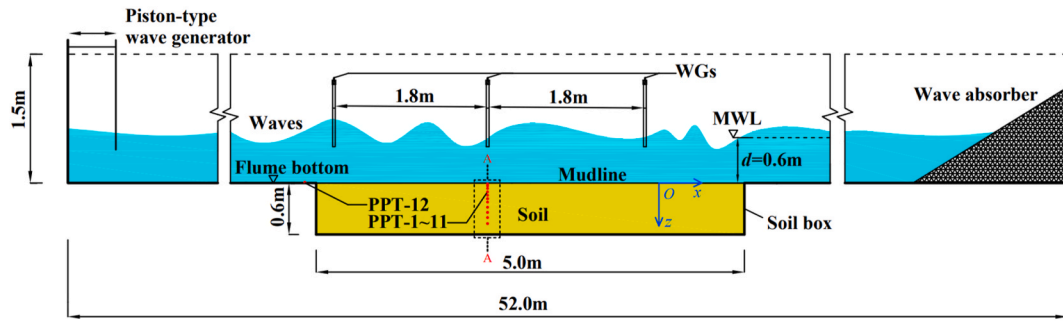
(a)
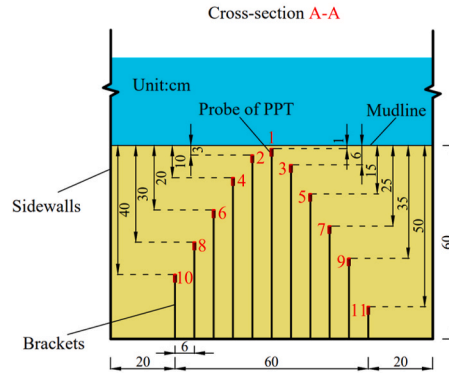


(b)

**Fig. 1.** (a) Schematic diagram of the experimental set-up (MWL is the abbreviation for Mean Water Level); (b) Cross- section A-A: arrangement of PPTs within the sand bed.
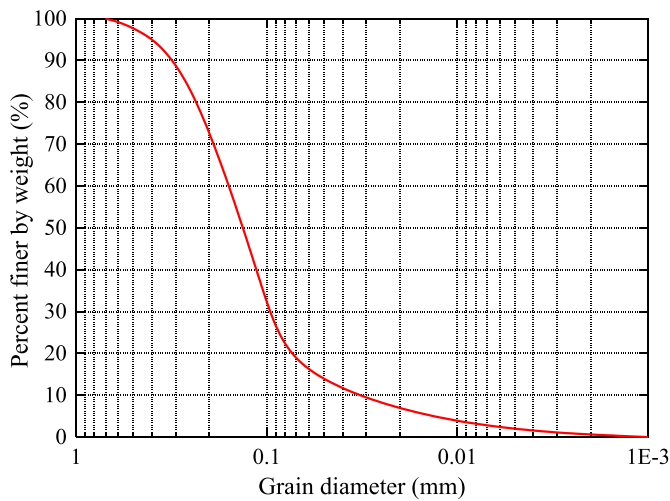


**Fig. 2.** Particle size distribution curve of the fine-sand.

**Table 1**
Main physical properties of the fine-sand.

| Soil properties | Symbols (Units) | Values |
| --- | --- | --- |
| Mean size of grains | $d_{50}$ (mm) | 0.12 |
| Effective size of grains | $d_{10}$ (mm) | 0.03 |
| Specific gravity of grains | $s$ | 2.65 |
| Buoyant unit weight | $\gamma'$ (N/m$^3$) | $9.70 \times 10^3$ |
| Coefficient of permeability | $k_s$ (m/s) | $9.60 \times 10^{-5}$ |
| Degree of saturation | $S_r$ | 0.993 |
| Void ratio | $e$ | 0.67 |
| Porosity | $n$ | 0.40 |
| Relative density | $D_r$ | 0.62 |
| Shear modulus | $G$ (MPa) | 23.8 |
| Poisson's ratio | $\nu$ | 0.30 |

1.7 cm in length, with the measuring range of 0–20 kPa and an accuracy of 0.2%, and the sampling frequency $f_s = 25$ Hz. To monitor the elevations of the free water surface, three wave gauges (WGs) were utilized down-wave from, just above, and up-wave from the location of the PPTs, respectively. These analog signals of the random-waves measured with WGs and the corresponding transient pore pressures measured with PPTs were sampled synchronously.

### 2.2. Generation of random-waves with JONSWAP spectra

The elevations of the free water surface of random-waves in the time domain ($\eta$) can be uniformly expressed as (see Stewart, 2006):

$$\eta(x, y, t) = \sum_{n=1}^{\infty} \sum_{m=1}^{\infty} A_{mn} \exp\{i[\lambda_n(x \cos\theta_m + y \sin\theta_m) + 2\pi f_n t + \varphi_{mn}]\} \quad (1a)$$

where $\lambda_n$ is the wave number of each wave component, $f_n$ is the frequency, $\varphi_{mn}$ is the initial phase angle, $\theta_m$ is the azimuth angle, $A_{mn}$ is the amplitude, and $i$ is the imaginary unit. In the present flume tests, the generated random-waves propagated unidirectionally along the $x$ axis (see Fig. 1(a)), thus Eq.(1a) can be simplified as:

$$\eta(x, t) = \sum_{n=1}^{\infty} A_n \exp\{i[\lambda_n x + 2\pi f_n t + \varphi_n]\} \quad (1b)$$

In the frequency domain, the energy spectrum of random-waves with a JONSWAP spectrum can be expressed uniformly as (see Goda, 2000):

$$S(f) = \beta_J H_s^2 T_p^{-4} f^{-5} \exp\left[ -1.25 \left(T_p f\right)^{-4} \right] \gamma^{\exp\left[ -\left(T_p f - 1\right)^2 / \left(2\sigma^2\right) \right]} \tag{2}$$

where $\beta_J = 0.0624 / [0.230 + 0.0336\gamma - 0.185(1.9 + \gamma)^{-1}(1.094 - 0.01915 \ln \gamma)]$; $T_p \simeq T_s / [1 - 0.132(\gamma + 0.2)^{-0.559}]$; $T_s$ is the significant wave period; $H_s$ is the significant wave height; $\sigma \simeq 0.07$ when $f \leq 1/T_p$, while $\sigma \simeq 0.09$ when $f > 1/T_p$; $\gamma$ is the parameter denoting the enhancement of the spectral peak. The values of $\gamma$ are generally within the range of 1.0–7.0 with the mean value of 3.3 determined from the data at the North Sea. In the present simulation, $\gamma$ is adopted as 3.3.

The main input parameters for the generation of random-waves are $H_s$, $T_s$, and $\gamma$. The significant parameters $H_s$ and $T_s$ are defined as the average wave height and wave period of the highest 1/3 individual waves, respectively, i.e., $H_s = \frac{1}{N/3} \sum_{i=1}^{N/3} H_i$, $T_s = \frac{1}{N/3} \sum_{i=1}^{N/3} T_i$. Another random-seed parameter (i.e., the initial phase angle $\varphi_{mn}$) should be determined before the wave generator was activated. Whereas unlike the crucial parameters aforementioned, the random-seed was not set intentionally. The spectrum expression in Eq. (2) excludes the initial phase angle ($\varphi_{mn}$) which appears explicitly in Eq. (1) since it may not affect the energy distribution of random-waves in the frequency domain (Zakharov et al., 2012). Moreover, the time-duration of a complete random-wave train was set as 20.48 s repeating several times during each test process. Such time-duration could provide an adequate number of individual waves comprising a full frequency spectrum of random-waves in a single wave group (see Section 3.2.1) and offer the mathematical simplicity for conducting Fast Fourier Transform.

Once the random-wave parameters were input and the wave generator in the flume was activated, the Inverse Fourier Transform (IFT) was conducted automatically to expand the target spectrum into controlling signals of voltage-time series. The series of analog signals then drove the piston's push-pull motion to produce random-waves with the target spectrum through the servo motor (see Schäffer, 1996). To guarantee the accuracy of wave spectra, a typical iterative linear correction to the simulating results should be implemented (Canard et al., 2022):

$$S^*(f) = S(f) + \delta[DS(f) - S(f)] \tag{3}$$

where $S^*(f)$ is the corrected spectrum; $S(f)$ is the measured spectrum; $\delta$ is the correction parameter; and $DS(f)$ is the target spectrum. The procedure was repeated until the error is relatively small or under tolerance. In general, an acceptable simulation of the target wave spectrum could be attained by repeating Eq. (3) less than three times.

Five series of random-wave flume tests are summarized in Table 2, where $H_m$ is the maximum wave height measured in the wave trains with JONSWAP spectra. The generated random waves were sustained for approximately 3.0 min in each test. During the random-wave loading, the mudline of the sand bed was monitored with a video camera, indicating that the soil surface kept almost unchanged, i.e., only tiny sand-ripples were observed and no apparent consolidation was detected. About 45 s after the wave generator was activated, the waveform and wave-induced pore pressures would stay practically

**Table 2**
**Random-wave parameters of the flume tests\*.**

| Test series | Wave parameters | | |
| --- | --- | --- | --- |
| | $H_m$ (cm) | $H_s$ (cm) | $T_s$ (s) |
| 1–1 | 12.8 | 12.0 | 1.2 |
| 1–2 | 12.7 | 12.0 | 1.5 |
| 1–3 | 12.1 | 12.0 | 1.8 |
| 1–4 | 17.2 | 15.0 | 1.5 |
| 1–5 | 9.3 | 9.0 | 1.5 |

\* **Note:** For comparisons, the regular-waves were generated with the same wave values as the significant parameters for random-waves ($H = H_s$, $T = T_s$).

stationary until the cessation of wave loading.

Regular-waves were generated with the same values of wave height and wave period as the significant values for the random-waves, i.e., $H = H_s$, $T = T_s$ (see Table 2). The comparison of the measured transient pore pressures between random and regular waves will be made in Section 3.1.

## 3. Results and discussions

### 3.1. Time-domain pore pressure responses under random-waves: comparisons with regular-waves

To better understand the distinctive features of excess pore pressures in a sandy seabed under random-waves, the measured data under random-waves are compared with analytical predictions under regular-waves. The time developments of random-wave surface elevations ($\eta$) and the corresponding excess pore pressures ($p$) at various soil depths for two values of significant wave period ($T_s$), i.e., $T_s = 1.2$ s, and 1.8 s, are shown in Fig. 3(a) and (b), respectively. Accordingly, Fig. 4(a) and (b) show the free water surface elevations ($\eta$) and the corresponding excess pore pressures ($p$) induced by regular-wave counterparts for $T = 1.2$ s, and 1.8 s, respectively. The time developments of free surface elevations ($\eta$) and the excess pore pressures ($p$) at a certain soil depth ($z = 0$, and 10.0 cm) induced by random-waves and regular-waves respectively were compared in Fig. 5 under the same wave conditions ($T_s = 1.2$ s and $H_s = 0.12$ m).

As can be anticipated, the transient pore pressures in the bed beneath induced by the monochromatic regular-waves remained sinusoidal (see Figs. 4 and 5). The amplitude-attenuation and phase-lag phenomena of pore pressures were observed under both the random (Fig. 3) and the regular-waves (Fig. 4). Nevertheless, the profiles of both the random-wave free surface elevations and the transient pore pressures induced are featured with conspicuous irregularity, as shown in Figs. 3 and 5. Moreover, the details of the pore pressure profiles in the sand bed are markedly different from those of the water surface profiles. The high-frequency components of the random-waves were not detected simultaneously by the pore-pressure transducers in the underlying soil layers (see the marked elliptical zones in Fig. 3). Such observations elicit that there may exist incongruous spatial distributions of pore pressures along the soil depth induced by the diverse monochromatic components within a wave train of random-waves.

As aforementioned, the analytical solution derived by Yamamoto et al. (1978) for predicting transient pore pressures in a poro-elastic seabed under regular-waves can be expressed as

$$p(z) = p_b \left[ (1-\alpha)e^{-\lambda z} + \alpha e^{-\lambda' z} \right] \tag{4a}$$

where $p_b$ is wave pressure at the seabed surface:

$$p_b = \frac{H\gamma_w}{2\cosh(\lambda d)} \exp[i(\lambda x - \omega t)] \tag{4b}$$

$H$ is the wave height of regular-waves; $\gamma_w$ is the unit weight of water; $\lambda$ is the wave number; $d$ is the water depth; $i$ is the imaginary unit; $\omega$ ($=2\pi f$) is the angular frequency of waves; $\alpha = \frac{im\omega''}{-\lambda'' + i(1+m)\omega''}$; $(\lambda')^2 = \lambda^2 + i\frac{\gamma_w}{k_s}\frac{\omega}{K}$; $m = \frac{nG}{(1-2\nu)K'}$; $\lambda'' = \frac{\lambda' - \lambda}{\lambda}$; $\omega'' = \frac{1-\nu}{1-2\nu}\frac{\omega'}{\lambda^2}$; $\omega' = \frac{\omega \gamma_w}{k_s K}$; $G$ is the shear modulus of the soil; $n$ is the porosity of the soil; $k_s$ is the coefficient of permeability; $\nu$ is the Poisson's ratio of the soil; $K'$ is the apparent bulk modulus of pore-fluid (Verruijt, 1969):

$$K' = \left( \frac{1}{K_w} + \frac{1-S_r}{P_0} \right)^{-1} \tag{5}$$

in which $K_w = 1.9 \times 10^9$ Pa is the true bulk modulus of water; $S_r$ is the degree of saturation; $P_0$ is the absolute hydrostatic pressure; and $K$ is the apparent bulk modulus of the poro-elastic bed:
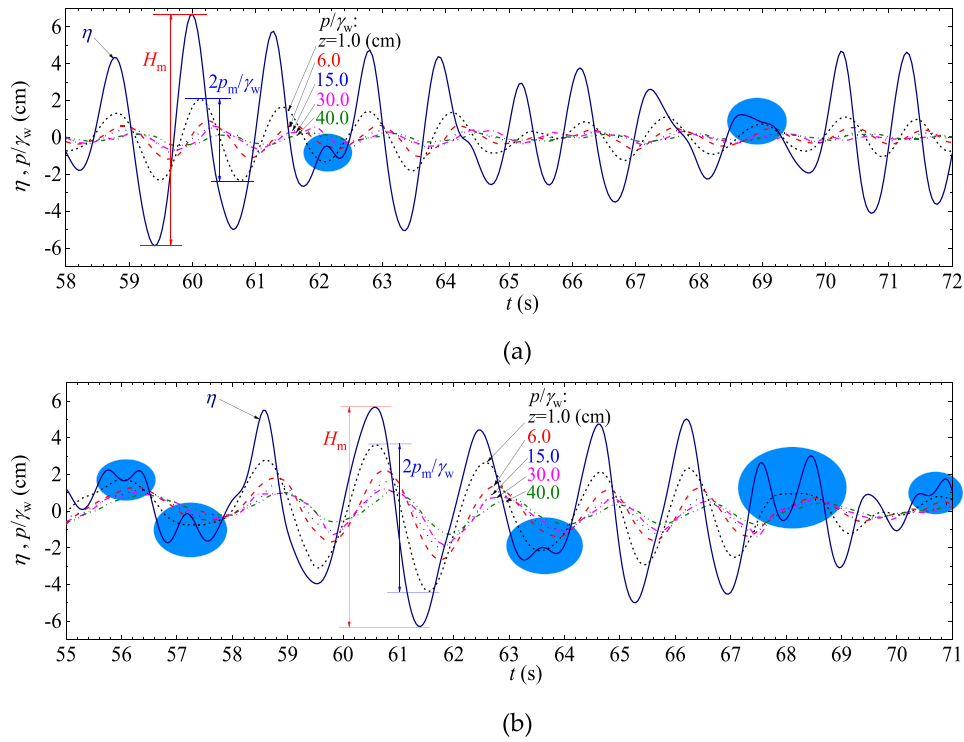
**Fig. 3.** Time developments of free surface elevation ($\eta$) and the corresponding excess pore pressure ($p$) at various soil depths under random-waves with JONSWAP spectra ($d = 0.6$ m, $H_s = 0.12$ m): (a) $T_s = 1.2$ s (Test 1-1); (b) $T_s = 1.8$ s (Test 1–3).
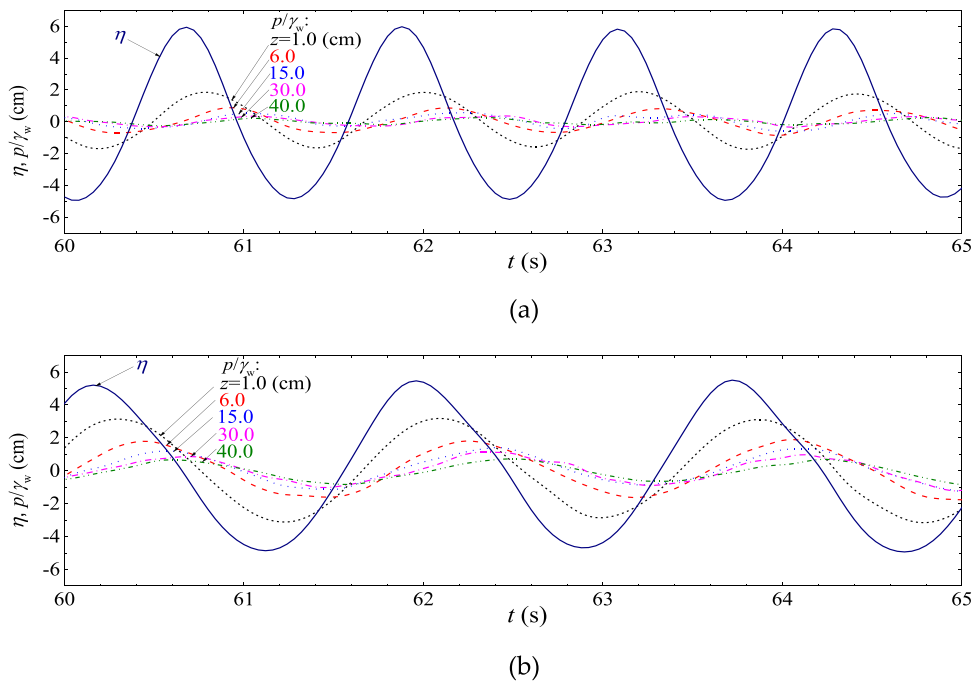


**Fig. 4.** Time developments of free surface elevation ($\eta$) and the corresponding excess pore pressure ($p$) at various soil depths under regular-waves ($d = 0.6$ m, $H = 0.12$ m): (a) $T = 1.2$ s; (b) $T = 1.8$ s.

$$K = \left( \frac{n}{K'} + \frac{1 - 2\nu}{2(1 - \nu)G} \right)^{-1} \quad (6)$$

$$R_k = \frac{2n(1 - \nu)G}{(1 - 2\nu)K'} \quad (7)$$

To evaluate the relative rigidity of soil-skeleton to pore-fluid, the parameter $R_k$ was introduced by Li and Gao (2022):

Given the soil properties of the fine-sand in Table 1, one can subsequently obtain that $R_k \gg 1.0$ and combining the wave parameters of the test conditions in Table 2 implies $\alpha \to 1.0$ (see Li and Gao, 2022). Then
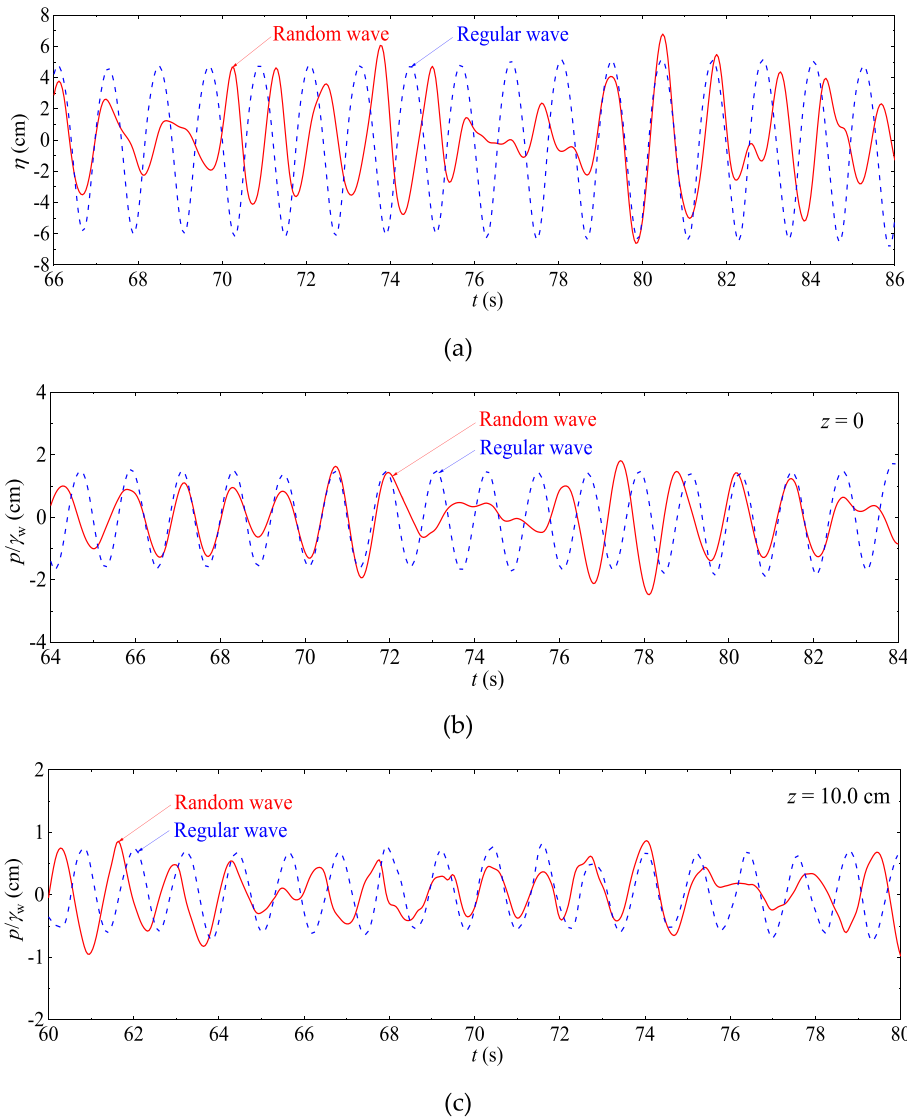
**Fig. 5.** Comparisons between random-waves and regular-waves ($d = 0.6$ m, $T_s = 1.2$ s, $H_s = 0.12$ m): (a) free surface elevations ($\eta$); (b) excess pore pressure ($p$) at z = 0 (mudline) and (c) that at z = 10.0 cm.

Eq.(4a) can be simplified as:

$$p(z) = \frac{\gamma_w H}{2\cosh(\lambda d)}\exp(-\lambda' z)\exp[i(\lambda x - \omega t)] \tag{8}$$

Note that the first natural exponential of Eq. (8) implies the amplitude-attenuation and the phase-lag of pore pressures along the soil depth, and the second one represents the regular traveling wave. As $(\lambda')^2 = \lambda^2 + i\frac{\gamma_w}{k_s}\frac{\omega}{K}$, Eq. (8) can be further intuitionally expressed as

$$p(z) = \frac{\gamma_w H}{2\cosh(\lambda d)}\exp(-\xi_1 z)\exp[i(\lambda x - \omega t - \xi_2 z)] \tag{9}$$

in which, the parameters $\xi_1$ and $\xi_2$ are explicitly expressed as

$$\xi_1 = \frac{\sqrt{2}}{2}\lambda\sqrt{1 + \sqrt{1 + \left(\frac{2\pi f \gamma_w}{\lambda^2 k_s K}\right)^2}} \tag{10}$$

$$\xi_2 = \frac{\sqrt{2}}{2}\lambda\sqrt{-1 + \sqrt{1 + \left(\frac{2\pi f \gamma_w}{\lambda^2 k_s K}\right)^2}} \tag{11}$$

Obviously, $\xi_1$ is the real attenuation rate of pore-pressure amplitude, and $\xi_2 z$ is the phase-lag. The analytical expression for the amplitude of

the transient pore pressure ($p_m$) can subsequently be obtained:

$$p_m(z) = \frac{\gamma_w H}{2\cosh(\lambda d)}\exp(-\xi_1 z) \tag{12}$$

It should be noted that the input wave parameters for calculating analytical predictions of $p_m$ with Eq. (12) are set as: $H = H_m$ or $H_s$, $T = T_s$ (see Table 2). In terms of the experimental results, $p_m$ is identified as half the maximum vertical difference between the wave crests and their adjacent wave troughs in a complete wave train (as marked in Fig. 3).

Comparisons of the pore-pressure amplitude ($p_m$) in the time domain are made between the experimental results for random-waves and the analytical predictions for regular-waves (see Fig. 6). As shown in Fig. 6, the experimental results for regular-waves generally match well with the analytical predictions with Eq. (12). In deeper layers of the bed, the experimental results for regular-waves are slightly larger than the analytical predictions, which could be attributed to the boundary effects from the flume bottom. Nevertheless, the experimental results for random-waves deviate from the predicted values, especially in the deeper layers (see Fig. 6). Note that only the significant wave period ($T_s$) could be taken into account in the conventional analytical predictions, i. e., the influence of the remaining wave-period components of random-waves was ignored. This motivated the authors to further examine the
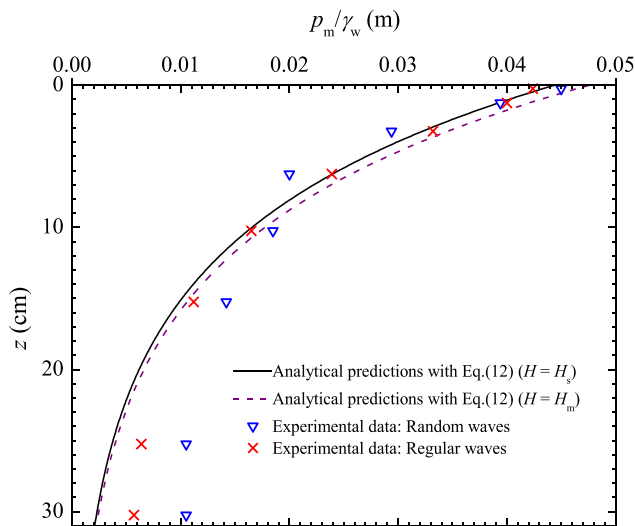
**Fig. 6.** Comparisons between experimental data and analytical predictions of both random and regular wave-induced pore-pressure amplitude ($p_m$) at various soil depths (Test 1–4: JONSWAP spectrum; $d = 0.6$ m, $H_s = 15$ cm and $T_s = 1.5$ s).

random-wave induced pore pressure response in the frequency domain by spectral analyses.

### 3.2. Fourier analyses of the pore-pressure responses under random-waves

#### 3.2.1. Response spectra of pore pressures: secondary spectral peak

In this section, the transient pore-pressure responses in the frequency domain are investigated by employing the method of Fourier analysis. We took one complete period of wave train (i.e., 20.48 s) and then conducted the Fast Fourier Transform (FFT) by setting the parameter $N_{FFT} = 512$ (the spectral frequency resolution $\Delta f = f_s/N_{FFT} \approx 0.0488$ Hz) to obtain the frequency spectra (Cooley and Jukey, 1965). Finer resolution could be inconsistent with the accuracy of the mechanical setting of the wave generator, even though the refinement can be achieved mathematically. The horizontal axis of the spectrum represents the frequencies of various wave components, while the vertical axis corresponds to the energy density ($E$) that is proportional to the square of amplitude density. As the expression $p/\gamma_w$ has the same dimension with $\eta$ (i.e., cm), the dimension of $E$ in pore-pressure spectra should be consistent with that in wave spectra (i.e., $\times 10^{-4} m^2$/Hz).

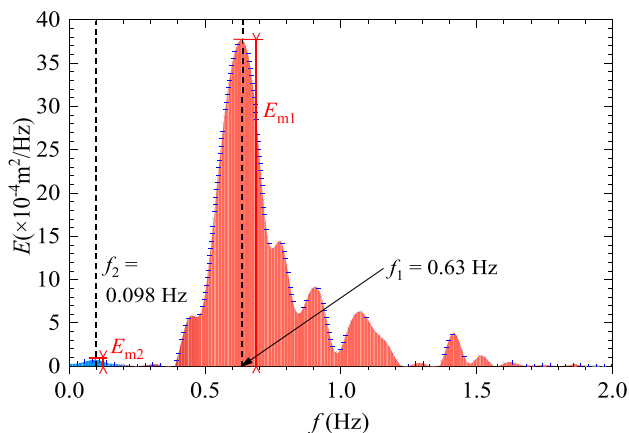A frequency spectrum of the generated random-waves with a typical



**Fig. 7.** Frequency spectrum of the random-waves with JONSWAP spectrum (Test 1–4: $d = 0.6$ m, $H_s = 15$ cm and $T_s = 1.5$ s).

JONSWAP spectrum is demonstrated in Fig. 7. As the wave generator actually produced finite discrete wave components in a single wave train, the JONSWAP spectrum with modest fluctuations was eventually simulated due to the slight unsteadiness and nonlinearity of the waveform, especially in high-frequency zones. The wavelet transform can be recommended so as to further denoise the spectrum (Barclay et al., 1997; Hsieh, 2001; Karshenas et al., 1999; Wang and Tang, 2010).

Correspondingly, the response spectra for transient pore pressures at various soil depths (i.e., $z = 1.0$ cm, 10.0 cm, 25.0 cm, 40.0 cm, and 50.0 cm) in the sand bed under random-waves are given in Fig. 8(a)-(e). As shown in Fig. 8, the dominant dual-peaks, i.e., a high-frequency primary peak ($E_{m1}$) and a low-frequency secondary peak ($E_{m2}$) can be generally identified from the pore-pressure spectra. The primary peak frequency ($f_{p1}$, briefly noted as $f_1$) of the random-waves is approximately equal to the significant wave frequency $f_s$ ($= 1/T_s$). The secondary spectral peak possibly represents the group-bounded infragravity wave, which has much longer wavelengths and smaller amplitudes than typical gravity waves (Bertin et al., 2018). The group-bounded waves were also observed in the flume tests of Schäffer (1996). Longuet-Higgins and Stewart (1962) ever investigated the slight depression and rise of mean water level bounded to a wave group (i.e., the infragravity wave) and termed such effect as the "radiation stress" ascribed to the second-order Stokes interactions. The group-bounded long wave is graphically manifested as the asymmetry between surface wave crests and troughs in the present flume tests (see Fig. 3). According to Longuet-Higgins and Stewart (1962), the group-bounded long wave travels phase-locked to the wave group, thus the frequencies of the long wave ($f_{gb}$) can be determined as:

$$f_{gb} = nf_{wg}, n = 1, 2, \cdots \qquad (13)$$

where $f_{wg}$ is the frequency of the envelope of the wave group. Note: $f_{wg}$ is equal to the reciprocal of the period of the wave group ($T_{wg}$), i.e., $f_{wg} = 1/T_{wg}$. Various values of $n$ in Eq. (13) represent the base-frequency component and higher-order harmonic components of the group-bound wave, among which the base-frequency and the second-order harmonic component ($n = 1$ and 2) are commonly identified in the present flume tests. With a complete wave train lasting for $T_{wg} = 20.48$ s, we have $f_{wg} = 0.049$ Hz. It is indicated that, in the random-wave spectrum and pore-pressure spectra for various soil depths, the secondary peak frequency ($f_{p2}$, briefly noted as $f_2$) is 0.098 Hz (see Figs. 7 and 8), so we can obtain the frequency-matching equation:

$$f_2 = 2f_{wg} \qquad (14)$$

It is implied that the secondary spectral peak in the spectra (Figs. 7 and 8) might correspond to the second-order harmonic component of the group-bounded wave (i.e., $n = 2$ in Eq. (13)). As for the other test conditions, the frequency-matching states are exemplified graphically in Fig. 9 and summarized quantitatively in Table 3. Moreover, the measured group-bounded long wave in the time domain is shown in Fig. 10, demonstrating a relative depression of the mean water level under such a group of high random-waves. As such, it would be essentially convincing that the group-bounded long wave appears in the spectra as the secondary peak.

#### 3.2.2. Spectral bandwidth

After figuring out the generating mechanism of the secondary spectral peak (see Section 3.2.1), we manage to reveal the impacts of the long-wave components on pore-pressure responses in the seabed. For simplicity, it is assumed that the spectral peak could be represented by a monochromatic wave component with the peak frequency. Above all, some essential premises ought to be scrutinized, especially whether the spectra are narrow-banded. There exist four typical parameters to evaluate the spectral bandwidth for random-waves.
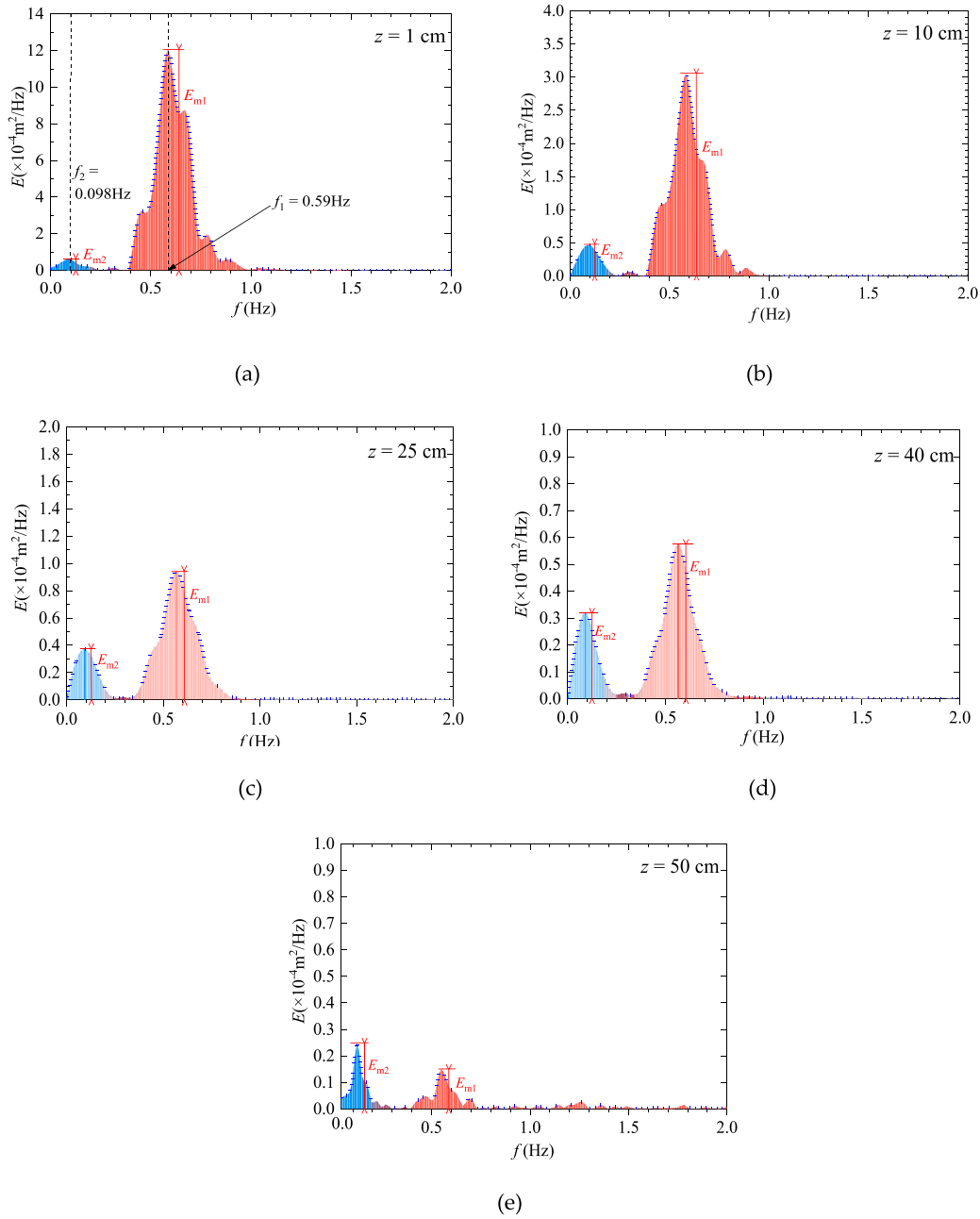
**Fig. 8.** Response spectra for random-wave induced pore pressures at various soil depths: (a) $z = 1$ cm; (b) $z = 10$ cm; (c) $z = 25$ cm; (d) $z = 40$ cm; (e) $z = 50$ cm (Test 1–4: JONSWAP spectrum; $d = 0.6$ m, $H_s = 15$ cm and $T_s = 1.5$ s).

(1) The spectral width parameter $\varepsilon_s$ was introduced by Cartwright and Longuet-Higgins (1956):

$$\varepsilon_s = \left(1 - \frac{m_2^2}{m_0 m_4}\right)^{1/2} \quad (\text{for } 0 < \varepsilon_s < 1) \tag{15}$$

where $m_i = \int_{LF}^{HF} f^i E(f) df$ is the $i$th spectral moment of the energy spectrum about the origin; *LF* and *HF* are the lower and higher cut-off frequencies, respectively. In general, $\varepsilon_s$ is a measure of the root mean square width of an energy spectrum. A spectrum is considered to be narrow-banded if $\varepsilon_s \to 0$, whereas it is broad-banded if $\varepsilon_s \to 1$.

(2) Another parameter is the spectral narrowness parameter $\nu_s$, which can be calculated from the spectral moments (see Longuet-Higgins, 1975):

$$\nu_s = \left(\frac{m_0 m_2}{m_1^2} - 1\right)^{1/2} \quad (\text{normally for } 0 < \nu_s < 1) \tag{16}$$

A spectrum is narrow-banded if $\nu_s \to 0$ and vice versa. It was remarked by Longuet-Higgins (1975) that $\nu_s$ was approximately half the value of the spectral width parameter $\varepsilon_s$ in Eq. (15) for a narrow-banded spectrum.

(3) From the zero-upcrossing method of wave analysis, Tucker (1963) proposed the spectral width parameter $\varepsilon_0$:

$$\varepsilon_0 = \left(1 - \frac{T_c}{T_z}\right)^{1/2} \quad (\text{for } 0 < \varepsilon_0 < 1) \tag{17}$$

where $T_c$ and $T_z$ are the mean crest period and the mean zero-upcrossing period (i.e., the mean time interval between the successive crest points
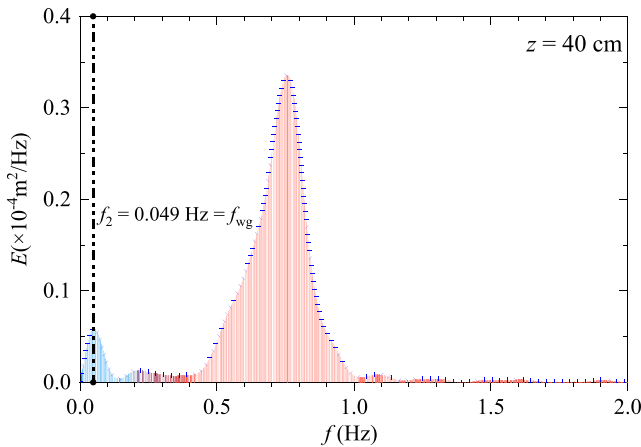
**Fig. 9.** Response spectrum of the random-wave induced pore pressures at $z = 40$ cm for another example of frequency-matching between $f_2$ and $f_{gb}$ (Test 1-1: JONSWAP spectrum; $d = 0.6$ m, $H_s = 12$ cm and $T_s = 1.2$ s).

**Table 3**
Frequency-matching states between $f_2$ and $f_{gb}$ for each test condition.

| Test series | $f_2$ (Hz) | Matching states | Representative order of harmonic components of the group-bounded long wave |
|---|---|---|---|
| 1–1 | 0.049 | $f_2 = f_{wg}$ | Base-frequency |
| 1–2 | 0.098 | $f_2 = 2f_{wg}$ | Second-order |
| 1–3 | 0.049 & 0.098 | $f_2 = f_{wg}$ & $f_2 = 2f_{wg}$ | Both base-frequency & second-order |
| 1–4 | 0.098 | $f_2 = 2f_{wg}$ | Second-order |
| 1–5 | 0.098 | $f_2 = 2f_{wg}$ | Second-order |

and between the successive zero-upcrossing points) in a wave group, respectively. A spectrum can be regarded as narrow-banded if $\varepsilon_0 \to 0$ and vice versa. Different from the above-mentioned parameters described with spectral moments in the frequency domain, $\varepsilon_0$ can be derived directly from the wave profile in the time domain.

(4) The spectral peakedness parameter $Q_p$ proposed by Goda (1970) can also reflect the bandwidth of spectral peaks:

$$Q_p = \frac{2\int_{LF}^{HF} f[E(f)]^2 df}{\left[\int_{LF}^{HF} E(f)df\right]^2} \text{ (normally for } 1 \le Q_p < \infty) \tag{18}$$

A spectrum is narrow-banded if $Q_p \to \infty$, whereas it is broad-banded if $Q_p \to 1$. For instance, $Q_p = (f_2 + f_1)/(f_2 - f_1)$ for a uniformly distributed

spectrum between frequencies $f_1$ and $f_2$ (see Goda, 1970). As such, $Q_p$ would vary with the horizontal translation of the distribution in the spectrum. Due to the existence of factor $f$ in the numerator of Eq. (18), $Q_p$ would never satisfy translation-invariance when the peak moves horizontally in the spectrum, which is physically fallacious for the evaluation of the spectral bandwidth.

With the elaboration of applicable situations for the aforementioned parameters for various types of spectra, it was concluded that the peakedness parameter $Q_p$ (Eq. (18)) is a preferred choice for diverse spectral forms (see Prasada Ran, 1988). Hence $Q_p$ is modified to describe the spectral bandwidth effect herein. Note that the statement that the apparent random-wave heights follow the Rayleigh distribution (as above-mentioned in Section 1) would not be accurately correct unless the spectrum is narrow-banded, despite the uncanny resemblance between the wave height distribution resulted from the zero-upcrossing method and the Rayleighan (Goda, 2000).

For the dual-peaked spectrum in the present study, the parameter $Q_p$ is modified as a translation-invariant and locally-defined quantity (i.e., $Q'_{p1}$ and $Q'_{p2}$) to describe the bandwidth of the two spectral peaks respectively. As such, $Q'_{p1}$ or $Q'_{p2}$ is obtained by ignoring the other peak (changing the cut-off frequencies $LF$ and $HF$) and modifying Eq. (18) as:

$$Q'_p = \frac{2\int_{LF}^{HF} (f + f_{ref} - f_p)[E(f)]^2 df}{\left[\int_{LF}^{HF} E(f)df\right]^2} \tag{19}$$

where the prime denotes the modified version; $f_p$ is the spectral peak frequency and $f_{ref}$ is the reference frequency, which should be selected appropriately. In fact, the modification of the spectral peakedness parameter translates all the spectral peaks consistently to the same fixed position corresponding to the reference frequency, thus satisfying translation-invariance. Herein the reference frequency is adopted as the primary peak frequency (i.e., $f_{ref} = f_1$) for convenience, then the parameters can be obtained explicitly:

$$Q'_{p1} = \frac{2\int_{LF}^{HF} f[E(f)]^2 df}{\left[\int_{LF}^{HF} E(f)df\right]^2} ; \quad Q'_{p2} = \frac{2\int_{LF}^{HF} (f + f_1 - f_2)[E(f)]^2 df}{\left[\int_{LF}^{HF} E(f)df\right]^2} \tag{20}$$

Without ambiguity, spectral normalization is an inherent property of the fraction in Eq. (19), ensuring the feasibility of the modification above. The systematic examination indicates that $Q'_{p1}$ and $Q'_{p2}$ of the present experiments are much larger than unity (see Table 4). Practically, the resonant interaction (e.g., Hasselmann, 1962), the Benjamin-Feir instability (e.g., Benjamin and Feir, 1967), and other nonlinear interactions might lead to a somewhat wider wave spectrum, which accounts for the present deficiency of strictly narrow-banded spectra.
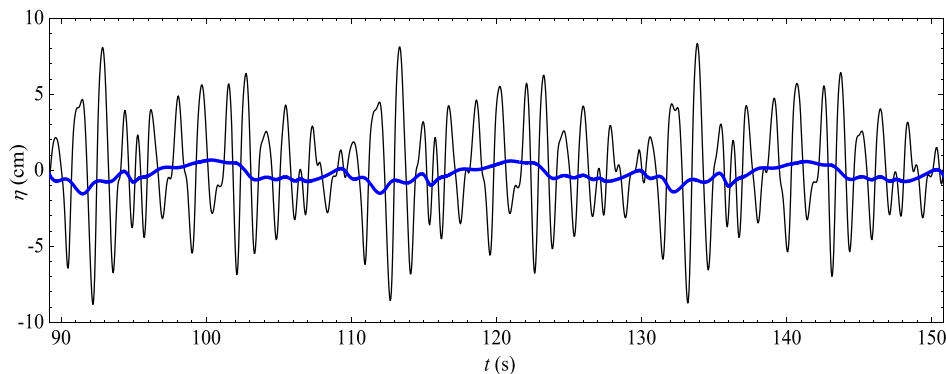


**Fig. 10.** Time series of free water surface elevations (in black) and the group-bounded long wave (in blue) as extended as 3 complete periods of wave trains (Test 1–4: JONSWAP spectrum; $d = 0.6$ m, $H_s = 15$ cm and $T_s = 1.5$ s).

**Table 4**

Spectral peakedness parameters ($Q'_{p1}$ and $Q'_{p2}$) of the dual-peaked spectra for random-waves and the corresponding pore pressures at various soil depths (Test 1–4: JONSWAP spectrum; $d = 0.6$ m, $H_s = 15$ cm and $T_s = 1.5$ s).

| Spectra | $H$ | $z = 0$ m | $z = 0.01$ m | $z = 0.03$ m | $z = 0.06$ m | $z = 0.10$ m |
|---|---|---|---|---|---|---|
| $Q'_{p1}$ | 3.27 | 4.29 | 3.87 | 3.86 | 3.81 | 3.82 |
| $Q'_{p2}$ | 5.63 | 7.94 | 5.96 | 6.92 | 6.40 | 7.21 |
| Spectra | $z = 0.15$ m | $z = 0.25$ m | $z = 0.30$ m | $z = 0.35$ m | $z = 0.40$ m | $z = 0.50$ m |
| $Q'_{p1}$ | 3.92 | 3.76 | 3.88 | 4.11 | 4.08 | 4.23 |
| $Q'_{p2}$ | 6.16 | 6.98 | 8.31 | 7.71 | 7.58 | 5.24 |

### 3.2.3. Frequency-filtering effects

For a narrow-banded spectrum with dual peaks, random-waves can be simply regarded as a linear superposition of such two harmonic (sinusoidal) wave components corresponding to the two spectral peaks. Compared with the primary peak, the magnitude of the secondary peak is much lower in the wave spectrum (approximately 2% of the primary peak, see Fig. 7). Nevertheless, the secondary peak is no longer negligible in relatively deeper soil layers (see Fig. 8(b)–(e)).

Fig. 11 intuitively gives the comparisons between the two spectral peaks ($E_{m1}$ and $E_{m2}$) along the soil depth. It is indicated that the attenuation of the primary peak is quite rapid while the secondary peak with a lower frequency attenuates remarkably slowly. As such, the soil would behave like a filter: the pore pressures induced by short-wave components are more easily filtered by the soil; while those induced by long-wave components are apt to propagate downwards to the deeper soil layers. Due to such "frequency-filtering" effects, the response spectra at deeper locations would be profoundly different from those at the shallower soil layers. The low-frequency secondary peak would gradually surpass the high-frequency primary peak with increasing soil depth and end up with prevailing in the frequency domain of pore pressures. The shift between spectral peaks may be attributed to the different abilities of transmission within the soil for the two wave components with different frequencies, which is analytically implied in Eq. (9). As indicated by Niu et al. (2019), long-wave components in the random-wave spectrum tend to perform more severely in the pore-pressure responses, thus both peaks may make non-negligible contributions to the pore pressures in the seabed. This also accounts for the fact that pore-pressure amplitudes induced by random-waves are evidently larger than those induced by regular-waves in deep soil layers (see Fig. 6). That



**Fig. 11.** Vertical distributions of the primary peak ($E_{m1}$) and the secondary peak ($E_{m2}$) along the soil depth (Test 1–4: JONSWAP spectrum; $d = 0.6$ m, $H_s = 15$ cm and $T_s = 1.5$ s).

is, the impact of the low-frequency secondary peak (i.e., the long-wave component) may be indiscriminately discarded if random-waves are characterized by monochromatic regular-waves with significant wave parameters, and the analytical solution of Yamamoto et al. (1978) is then applied. Without ambiguity, the soil depth where $E_{m1} = E_{m2}$ represents an equivalence of the energy of two corresponding wave-induced pore-pressure components.

Unlike the traditional spectra for the random processes (e.g., ocean-wave spectra and seismic spectra), the present spectra for the pore-pressure (see Fig. 8) gradually evolve along the soil depth and exhibit several particularities. As above-stated in Section 1, long-wave components are universal in the real ocean environments. From a fundamental perspective, the physical modeling herein utilized a secondary-peak in the wave spectrum to reflect the major impacts of long-wave on pore-pressure responses. For such pore-pressure spectra with dual peaks, the various frequency components evolve downwards and compete with each other with the increase of soil depth, indicating the influence of long-wave gets much more significant in the deeper layers.

### 3.3. Filtering-depths: derivation and validation

To characterize the frequency-filtering effects of the seabed, the filtering-depth ($z_{1/n}$) is introduced, which is defined as the depth where the value of $E_{m2}$ reaches $1/n$ of the value of $E_{m1}$ (i.e., $E_{m2} = E_{m1}/n$). For instance, one can recognize that $E_{m2} = E_{m1}/2$ at $z = z_{1/2}$ (i.e., $n = 2.0$, which is marked with a red dot in Fig. 11). Generally, $n$ can be any positive integer or fraction herein. As $E_{m1}$ and $E_{m2}$ have the same order of magnitude at the filtering-depths for $n < 10.0$, the primary wave components (corresponding to the high-frequency $f_1$) and the secondary wave components (corresponding to the low-frequency $f_2$) both affect the pore-pressure responses within the seabed. Furthermore, the filtering-depths ($z_{1/n}$) can be determined explicitly by the ratio of $E_{m1}$ to $E_{m2}$ in the spectrum at a reference soil depth $z_{ref} = 1.0$ cm ($\kappa(1)$) and the two fixed corresponding frequencies ($f_1 > f_2$ in default). The derivations are concluded below.

It should be noted that the extremely high-frequency free surface wave or pore-pressure components (e.g., $f > 2.0$ Hz) in the spectra (see Figs. 7 and 8) are virtually negligible. As the lower frequency limit of the extremely high-frequency wave components can be set as 4.0 Hz (Mitsuyasu, 1977), the capillary effect could be neglected. Therefore, the random-waves can be regarded as surface gravity waves herein. Moreover, the ratio of the energy density in the spectrum is exactly equal to the square of the ratio of the corresponding wave or pore-pressure amplitudes, i.e., $E_{m1}/E_{m2} = (H_1/H_2)^2$ or $E_{m1}/E_{m2} = (p_{m1}/p_{m2})^2$. Consequently, the amplitude ratio of wave-induced pore-pressure components corresponding to the wave frequencies $f_1$ and $f_2$ at any soil depth can be derived from Eq. (12):

$$\frac{p_{m1}}{p_{m2}} = \sqrt{\kappa(z)} = \frac{H_1}{H_2}\frac{\cosh(\lambda_2 d)}{\cosh(\lambda_1 d)}\exp\{[\xi_1(f_2) - \xi_1(f_1)]z\} \tag{21}$$

where $\kappa(z) = E_{m1}/E_{m2}$ is the ratio of the primary peak to the secondary peak in the response spectrum at the soil depth $z$, and the amplitude-attenuation rate $\xi_1 = \frac{\sqrt{2}}{2}\lambda\sqrt{1 + \sqrt{1 + \left(\frac{2\pi f \gamma_w}{\lambda^2 k_s K}\right)^2}}$ (see Eq. (10)). Setting $z_{ref} = 0.01$ (m) as the reference soil depth, it can be derived that

$$\sqrt{\kappa(z)} = \sqrt{\kappa(1)}\exp\{[\xi_1(f_2) - \xi_1(f_1)](z - 0.01)\} \tag{22}$$

Substituting $z = z_{1/n}$ and $\kappa(z_{1/n}) = n$ into Eq. (22) gives

$$z_{1/n} = 0.01 + \frac{0.5}{\xi_1(f_1) - \xi_1(f_2)}\ln\frac{\kappa(1)}{n} \tag{23}$$

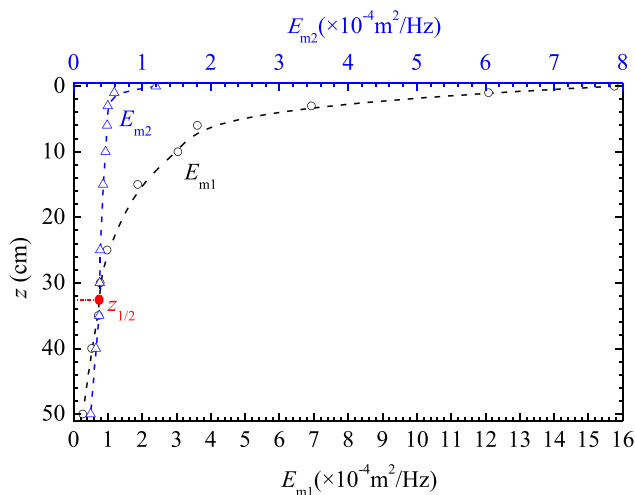and the wave parameters satisfy the dispersion relationship of linear surface gravity waves:

$$(2\pi f)^2 = g\lambda \tanh(\lambda d) \tag{24}$$

A non-dimensional parameter ($I_c$) was ever introduced by Li and Gao (2022) to characterize the combined effects of wave parameters and soil properties on pore-pressure responses:

$$I_c = \frac{2\pi f \gamma_w}{\lambda^2 k_s K} \tag{25}$$

Thereby, $\xi_1 = \lambda\sqrt{(1 + \sqrt{1 + I_c^2})/2}$ can be simplified as $\xi_1 = \lambda\sqrt{I_c/2}$ when $I_c \gg 1.0$, which can be approximately satisfied for the present flume tests (in the range of $10.0 < I_c < 1.0 \times 10^3$). Obviously, the non-dimensional parameter $I_c$ can be employed for evaluating the ability

of wave loading's transmission into the seabed compared with that within the water body.

The comparisons of the filtering-depths ($z_{1/n}$) between the analytical predictions with Eq. (23) and experimental data are shown in Fig. 12. It should be noted that the pore pressures were detected with the pore-pressure transducers discretely distributed along the soil depth (see the right longitudinal coordinates in Fig. 12(a)–(e)). As shown in Fig. 12, the data ranges of $z_{1/n}$ for various values of $n$ are evaluated based on the locations of the PPTs (see Fig. 1(b)). Good agreements are achieved between the analytical predictions and experimental data for $z_{1/n}$ (see Fig. 13). As such, if the random-wave induced pore-pressure responses in the time domain are acquired at any one certain depth ($z_{ref} = 1.0$ cm is chosen in the present study), one can directly obtain the two spectral
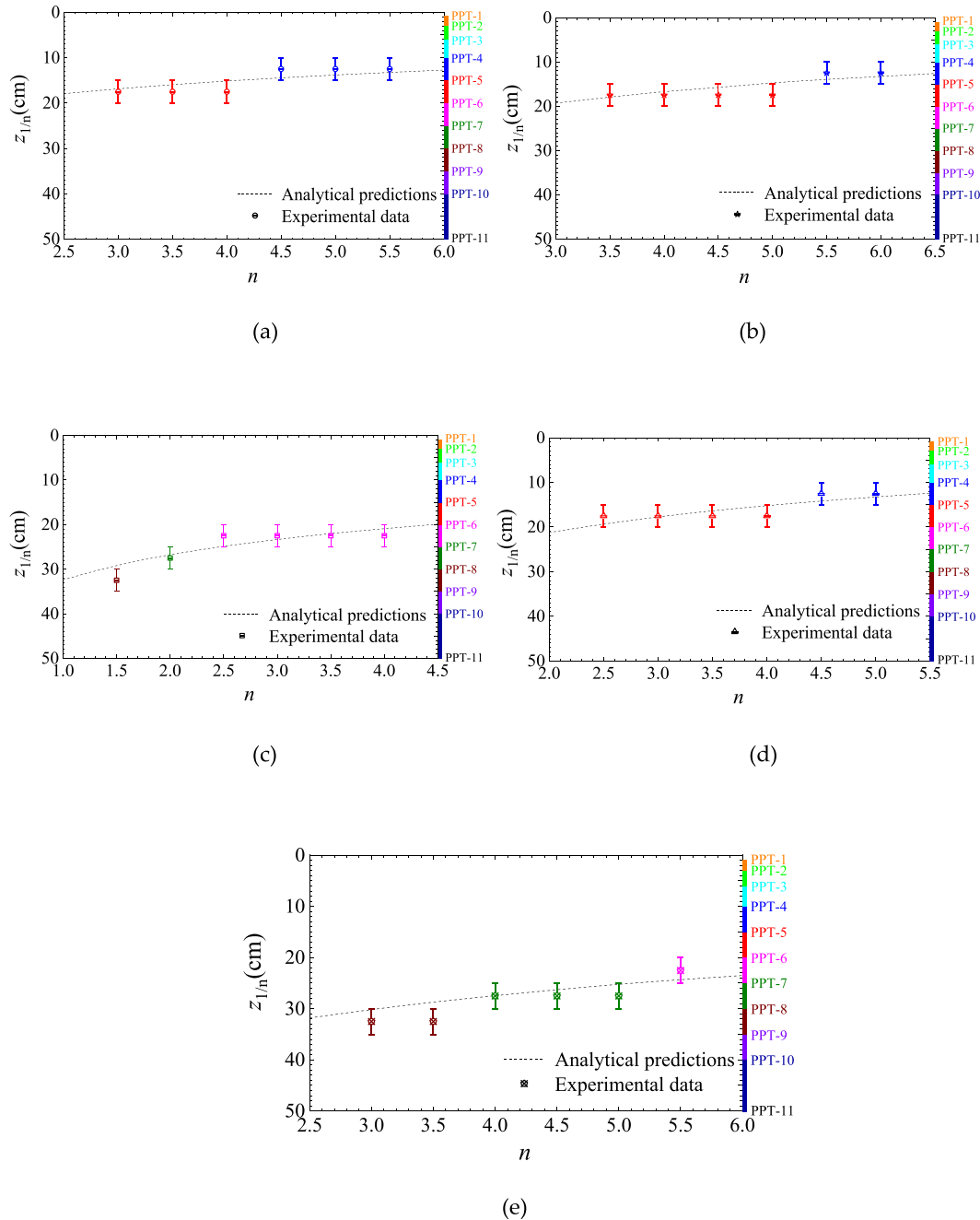


**Fig. 12.** Comparisons between the analytical predictions with Eq. (23) and experimental data of the filtering-depths ($z_{1/n}$) under various $n$ for the JONSWAP spectra: (a) Test 1-1: $H_s = 12$ cm, $T_s = 1.2$ s; (b) Test 1-2: $H_s = 12$ cm, $T_s = 1.5$ s; (c) Test 1-3: $H_s = 12$ cm, $T_s = 1.8$ s; (d) Test 1-4: $H_s = 15$ cm, $T_s = 1.5$ s; (e) Test 1-5: $H_s = 9$ cm, $T_s = 1.5$ s.
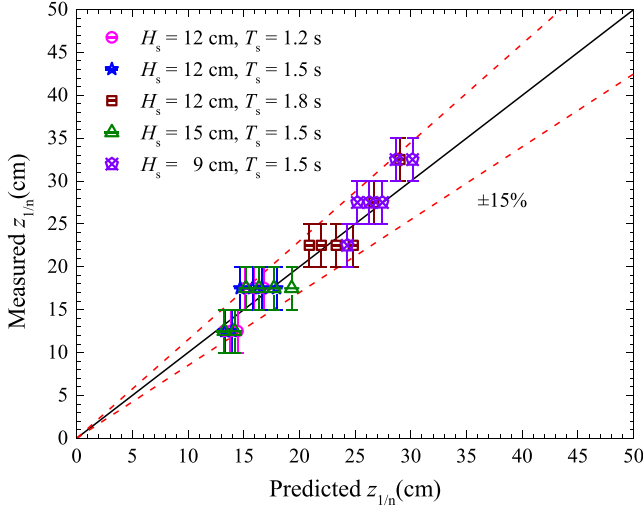
**Fig. 13.** Comparisons between the measured and predicted values of $z_{1/n}$ in all the tests.

peak frequencies ($f_1$ and $f_2$) and the initial energy ratio ($\kappa(z_{\text{ref}})$) through the method of Fourier analysis. Subsequently, the energy ratio of the two pore-pressure components at any other soil depths ($\kappa(z)$) and the filtering-depths ($z_{1/n}$) can be obtained in field trials via Eqs. (22 and 23), respectively.

## 4. Parametric analyses

To examine the key influential factors of the frequency-filtering phenomenon, parametric analyses are conducted in this section. Following the derivation of Eq. (23), the filtering-depths referencing the pore-pressure spectrum at the seabed surface ($z_{\text{ref}} = 0$) can be obtained as:

$$z_{1/n} = \frac{0.5}{\xi_1(f_1) - \xi_1(f_2)} \ln \frac{\kappa(0)}{n} \tag{26}$$

For the cases of $I_c \gg 1.0$, $\xi_1 = \lambda \sqrt{\frac{I_c}{2}}$, thus it follows that:

$$z_{1/n} = \frac{0.5}{\sqrt{\frac{\pi f_1 \gamma_w}{k_s K}} - \sqrt{\frac{\pi f_2 \gamma_w}{k_s K}}} \left( \ln \left. \frac{E_{m1}}{E_{m2}} \right|_{z=0} - \ln n \right)$$

$$= \frac{1}{\sqrt{\frac{4\pi f_s \gamma_w}{k_s K}} \left(1 - \sqrt{\frac{f_2}{f_1}}\right)} \left( \ln \left. \frac{E_{m1}}{E_{m2}} \right|_{z=0} - \ln n \right) \tag{27}$$

Note that the primary peak frequency $f_1$ is approximately equal to the significant wave frequency $f_s$, i.e., $f_1 \approx f_s$. Then Eq. (27) can be further simplified as the following non-dimensional form:

$$\lambda_s z_{1/n} = \frac{1}{\sqrt{2 I_c^{(s)}}} \frac{\ln (E_{m1}/E_{m2})_{z=0} - \ln n}{1 - \sqrt{f_2/f_1}} \tag{28}$$

where $\lambda_s$ is the significant wave number of random-waves calculated with the dispersion relationship (see Eq. (24)); the non-dimensional parameter $I_c^{(s)}$ adapted to random-waves can be calculated with Eq. (25) by substituting the significant wave parameters.

### 4.1. Effects of frequency spectra

Given a short-term wave surface elevation ($\eta$) in the time domain, the wave spectrum can be naturally obtained through FFT. The primary and secondary peak frequency ($f_1$ and $f_2$) can then be extracted from the

wave spectrum if the spectrum is approximately dual-peaked and narrow-banded. The significant frequency ($f_s$) can be either obtained from the mathematical statistics of random-waves, or empirically set equal to $f_1$ with little deviance. As aforementioned, the latter assumption ($f_s \approx f_1$) is adopted for simplicity. Furthermore, the significant wave number of random-waves ($\lambda_s$) is calculated with the dispersion relationship (see Eq. (24)), which is then utilized to non-dimensionalize the filtering-depth ($z_{1/n}$) as $\lambda_s z_{1/n}$.

In the parametric study, the wave parameters are set as follows: water depth $d = 10.0$ (m), significant wave height $H_s = 3.0$ (m), gravitational acceleration $g = 9.80$ (m/s$^2$), unit weight of water $\gamma_w = 9.80 \times 10^3$ (N/m$^3$), and the values of significant wave periods are varied as $T_s = 1.5, 3.0, 4.5, 6.0$ and $7.5$ (s). Thus, the corresponding values of significant wave frequencies are $f_s = 0.667, 0.333, 0.222, 0.167$ and $0.133$ (Hz), respectively; and the values of significant wave numbers are $\lambda_s = 1.79, 0.448, 0.206, 0.130$ and $0.096$ (m$^{-1}$), respectively. The soil properties are set as follows: the degree of saturation of the soil is $S_r = 0.956$, the other soil properties (including $n$, $\nu$, and $d_{50}$) are the same with those of the fine-sand in the present flume tests (see Table 1). Under such conditions, the simplified form for $I_c^{(s)} \gg 1.0$ can be employed since $I_c^{(s)} > 10.0$.

Fig. 14 shows the variations of $\lambda_s z_{1/n}$ with $n$ for various values of the secondary peak frequency $f_2 = 0.20, 0.10, 0.067, 0.050$ and $0.040$ (Hz) under the fixed values of $f_1 = 0.667$ Hz, $k_s K = 1025$ Nm$^{-1}$s$^{-1}$ and $(E_{m1}/E_{m2})_{z=0} = 10.0$. This figure demonstrates the influence of the peak frequency ratio ($f_2/f_1$) in a simple but effective way, considering the effect of $f_1$ ($= f_s$) is intricate since $f_s$ is also included in the non-dimensional parameter $I_c^{(s)}$. With increasing the values of $f_2/f_1$ (which is generally smaller than 1.0), $\lambda_s z_{1/n}$ increases remarkably, as illustrated in Fig. 14.

Fig. 15 shows the variations of the non-dimensional filtering-depths ($\lambda_s z_{1/n}$) with $n$ for various values of $(E_{m1}/E_{m2})_{z=0}$ under the fixed values of $T_s = 1.5$ s, $f_2/f_1 = 0.30$ and $k_s K = 1025$ Nm$^{-1}$s$^{-1}$. In the parametric study, the values of the peak ratio $(E_{m1}/E_{m2})_{z=0}$ (also denoted by $\kappa(0)$ as aforementioned) are varied as $(E_{m1}/E_{m2})_{z=0} = 18.0, 15.0, 12.0, 9.0$ and $6.0$, respectively. As indicated by Eq. (28) and Fig. 15, the energy peak ratio at the seabed surface $(E_{m1}/E_{m2})_{z=0}$ would affect the filtering-depths profoundly as a spatially initial condition. The filtering-depths ($\lambda_s z_{1/n}$) would increase with the increase of the initial gap $(E_{m1}/E_{m2})_{z=0}$.

### 4.2. Effects of the non-dimensional parameter $I_c^{(s)}$

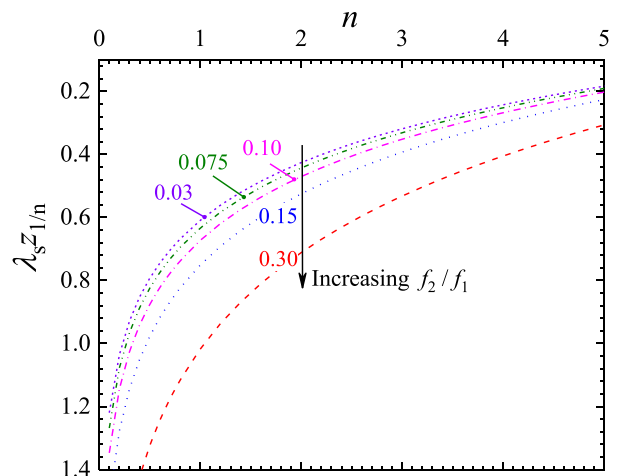As indicated in Eq. (25), $I_c^{(s)}$ is a parameter for the combined effects of



**Fig. 14.** Effects of secondary peak frequency ($f_2/f_1$) on filtering-depths: $\lambda_s z_{1/n}$ vs. $n$ ($f_1 = 0.667$ Hz, $k_s K = 1025$ Nm$^{-1}$s$^{-1}$ and $(E_{m1}/E_{m2})_{z=0} = 10.0$).
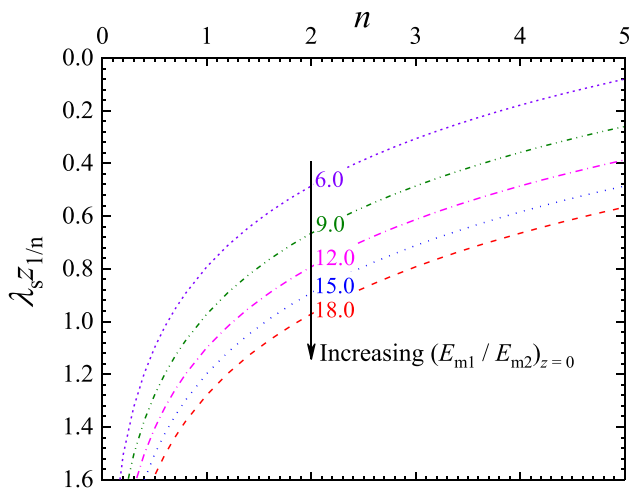
**Fig. 15.** Effects of peak ratio (the primary to the secondary peak) in the spectrum at the surface of the seabed $(E_{m1}/E_{m2})_{z=0}$ on filtering-depths: $\lambda_s z_{1/n}$ vs. $n$ ($T_s = 1.5$ s, $f_2/f_1 = 0.30$ and $k_s K = 1025$ Nm$^{-1}$s$^{-1}$).

both wave parameters and soil properties, which would comprehensively influence the filtering phenomenon. Both an increment of the significant wave period ($T_s$) and a decline of the combined soil rigidity-permeability parameter ($k_s K$) would lead to a consistent increase of the value of $I_c^{(s)}$. For non-cohesive soils, the values of permeability coefficient ($k_s$) and shear modulus ($G$) may vary dramatically from the fine silt to the coarse sand. The following values of the significant wave period ($T_s$) and the combined soil rigidity-permeability parameter ($k_s K$) are examined: $T_s = 1.5$ and $3.0$ (s); $k_s K = 1000, 500$ and $250$ (Nm$^{-1}$s$^{-1}$), respectively; six varied values of $I_c^{(s)}$ are thus examined: $I_c^{(s)} = 13, 26, 51, 102, 204,$ and $409$, respectively.

The effects of the non-dimensional parameter $I_c^{(s)}$ on the filtering-depths $\lambda_s z_{1/n}$ are shown in Fig. 16 for a fixed value of $(E_{m1}/E_{m2})_{z=0} = 15.0$. It should be noted that the frequency ratio keeps constant intentionally, i.e., $f_2/f_1 = 0.35$, even though $f_1 (= f_s)$ varies as an influential factor, which appears explicitly in the numerator and implicitly in the denominator of $I_c^{(s)}$ (see Eq. (25)). The orientation of the arrow in Fig. 16 reflects the increase of $I_c^{(s)}$, thus causing the decrease of $\lambda_s z_{1/n}$ (see Eq.
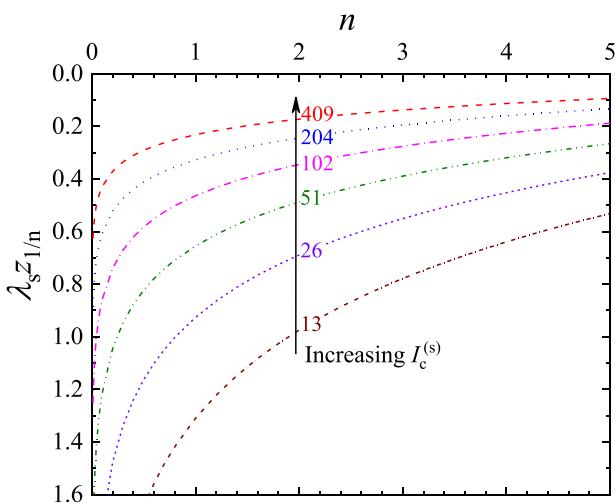
(28)). As such, for a given value of $n$, $\lambda_s z_{1/n}$ is proportional to $1/\sqrt{I_c^{(s)}}$ only if the response spectrum of pore pressures at the seabed surface is fixed. Namely, the non-dimensional parameter $I_c^{(s)}$ can be regarded as a scaling factor.

**Engineering implications**: As above stated, the real state of ocean waves is random in nature and composed of various monochromatic components. By merely considering a monochromatic component of random waves, traditional time-domain predictions may significantly underestimate the magnitude of transient pore pressures, particularly within deeper soil layers (see Fig. 6). Previous studies indicated that the seabed under the action of long waves is more prone to instantaneous liquefaction (see Sakai et al., 1992; Jeng, 1997; Qi and Gao, 2018). The present results show that, for typical pore-pressure spectra with dual-peaks, the secondary-peak (long waves) gets more significant in the deeper layers. Via the perspective of spectral analysis, the proposed filtering-depth and its influential factors may provide a quantitative characterization of such frequency-filtering effect, especially when predicting the liquefied soil depth under random waves.

## 5. Conclusions

In natural environments, ocean waves are random with various monochromatic components, which could lead to complex excess pore pressures in the seabed. Transient pore pressures in a fine-sand bed under the random waves with JONSWAP spectrum and the regular waves were physically modeled in a large wave flume, respectively. The following conclusions can be drawn from the flume observations and theoretical analyses.

(1) Monochromatic regular-wave induced transient pore pressures in the sand bed generally remain sinusoidal. Nevertheless, it was observed that the profiles of both random-wave surface elevations and the transient pore pressures are featured with conspicuous irregularity. The high-frequency components of the random-waves were not detected simultaneously by the pore-pressure transducers in the underlying soil layers, implying that pore pressures induced by various monochromatic components manifested incongruous spatial distributions along the soil depth. Comparisons between experimental data and analytical predictions indicate that the pore pressure responses under random-waves are profoundly distinctive from those under regular-waves, especially in deeper soil layers.

(2) By employing Fourier analysis, the response spectra are obtained for random-wave induced transient pore-pressures, based on which the frequency-filtering effect within a sand bed is identified. Two peaks were generally observed in the pore-pressure spectra, i.e., a primary peak (high-frequency) and a secondary peak (low-frequency). The frequency corresponding to the primary peak is approximately equal to the significant frequency of random-waves. It is speculated that the secondary spectral peak represents the group-bounded long wave through flume observation and quantitative matching with convincing accuracy. Investigation of the spectral bandwidth indicates that the present spectra are relatively narrow-banded. The primary spectral peak with high frequency attenuates more rapidly along the soil depth than the secondary spectral peak with low frequency. Consequently, the secondary spectral peak would gradually surpass the primary spectral peak with the increasing soil depth. Such frequency-filtering effects could be attributed to the different abilities of transmission within the soil for wave components of various frequencies.

(3) The filtering-depth ($z_{1/n}$) is proposed to quantitatively characterize the frequency-filtering effects. The analytically predicted filtering-depths are further validated with the experimental data. Parametric analyses indicate that both the pore-pressure



**Fig. 16.** Effects of the non-dimensional parameter $I_c^{(s)}$ on filtering-depths: $\lambda_s z_{1/n}$ vs. $n$ ($f_2/f_1 = 0.35$ and $(E_{m1}/E_{m2})_{z=0} = 15.0$).

spectrum at a reference soil depth and the non-dimensional parameter $I_c^{(s)}$ would have significant impacts on the filtering-depths. The non-dimensional filtering-depths $\lambda_s z_{1/n}$ increase with increasing the spectral peak ratio of a reference soil depth $\kappa(z_{ref})$ and the peak frequency ratio $f_2/f_1$, but with decreasing $I_c^{(s)}$. Given the time series of the transient pore pressures at a certain shallow soil depth and then utilizing the method of Fourier analysis, one can obtain the energy ratio of the two spectral peak wave components ($\kappa(z) = E_{m1}/E_{m2}$) at any other soil depths and the filtering-depths ($z_{1/n}$) in field trials.

## CRediT authorship contribution statement

**Jia-Hao Yu:** Writing – original draft, Experiments, Formal analysis, Derivations. **Fu-Ping Gao:** Conceptualization, Writing – review & editing, Supervision. **Chang-Fei Li:** Validation, Formal analysis.

## Declaration of competing interest

The authors declare that they have no known competing financial interests or personal relationships that could have appeared to influence the work reported in this paper.

## Data availability

No data was used for the research described in the article.

## Acknowledgements

## Notations

| | |
|---|---|
| $A_{mn}$ | Wave amplitude of each wave component |
| $d_{10}$ | Effective size of soil grains |
| $d_{50}$ | Mean size of soil grains |
| $D_r$ | Relative density of the soil |
| $DS(f)$ | Target spectrum of the wave generator |
| $e$ | Void ratio of the soil |
| $E$ | Energy density of the spectrum |
| $E_m$ | Peak value of the energy spectrum |
| $f$ | Frequency |
| $f_{gb}$ | Frequency of the group-bounded long wave |
| $f_n$ | Frequency of each wave component |
| $f_p$ | Peak frequency in the spectrum of the random-wave |
| $f_{ref}$ | Reference frequency in Eq. (19) |
| $f_s$ | Significant frequency of the random-wave |
| $f_{wg}$ | Frequency of the envelope of the wave group |
| $g$ | Gravitational acceleration |
| $G$ | Shear modulus of the soil |
| $d$ | Water depth |
| $H$ | Wave height |
| $H_m$ | Maximum wave height of the random-wave |
| $H_s$ | Significant wave height of the random-wave |
| $HF$ | Higher cut-off frequency in the spectrum |
| $i$ | Imaginary unit |
| $I_c$ | Non-dimensional parameter in Eq. (25) |
| $I_c^{(s)}$ | Non-dimensional parameter for the random-wave |
| $k_s$ | Coefficient of permeability of the soil |
| $K$ | Apparent bulk modulus of the poro-elastic soil |
| $K'$ | Apparent bulk modulus of the pore-fluid |
| $K_w$ | True bulk modulus of water |

| | |
|---|---|
| $LF$ | Lower cut-off frequency in the spectrum |
| $m$ | Coefficient in Eq. (4) |
| $m_i$ | $i$th spectral moment of the energy spectrum about the origin |
| $n$ | Soil porosity |
| $p$ | Transient pore pressure in the bed |
| $p_m$ | Amplitude of the transient pore pressure |
| $P_0$ | Absolute hydrostatic pressure at the seabed surface |
| $P_b$ | Wave pressure fluctuation at the seabed surface |
| $Q_p$ | Spectral peakedness parameter in Eq. (18) |
| $Q_p{}'$ | Modified spectral peakedness parameter in Eq. (19) |
| $R_k$ | Relative rigidity of soil-skeleton to pore-fluid in Eq. (7) |
| $s$ | Specific gravity of the soil grains |
| $S(f)$ | Measured spectrum of the wave generator |
| $S^*(f)$ | Corrected spectrum of the wave generator |
| $S_r$ | Degree of saturation of the soil |
| $t$ | Time |
| $T$ | Wave period |
| $T_c$ | Mean crest wave period in wave analysis |
| $T_s$ | Significant wave period of the random-wave |
| $T_p$ | Peak wave period in the spectrum of the random-wave |
| $T_{wg}$ | Period of the envelope of the wave group |
| $T_z$ | Mean zero-upcrossing wave period in wave analysis |
| $x$ | Streamwise coordinate |
| $y$ | Spanwise coordinate |
| $z$ | Soil depth calculated from the mudline |
| $z_{ref}$ | Reference soil depth in the filtering phenomenon |
| $z_{1/n}$ | Filtering-depth |
| $\lambda$ | Wave number |
| $\lambda_n$ | Wave number of each wave component |
| $\lambda_s$ | Significant wave number of the random-wave |
| $\gamma$ | Coefficient in Eq. (2) |
| $\gamma'$ | Buoyant unit weight of the soil |
| $\gamma_w$ | Unit weight of the water |
| $\omega$ | Angular frequency of the wave |
| $\omega'$ | Coefficient in Eq. (4) |
| $\omega''$ | Coefficient in Eq. (4) |
| $\varepsilon_s$ | Spectral width parameter in Eq. (15) |
| $\varepsilon_0$ | Spectral width parameter in Eq. (17) |
| $\nu$ | Poisson's ratio of the soil |
| $\nu_s$ | Spectral narrowness parameter in Eq. (16) |
| $\kappa(z)$ | Ratio of the primary to secondary peak of the spectrum at the depth $z$ |
| $\lambda'$ | Coefficient in Eq. (4) |
| $\lambda''$ | Coefficient in Eq. (4) |
| $\alpha$ | Coefficient in Eq. (4) |
| $\beta_J$ | Coefficient in Eq. (2) |
| $\sigma$ | Coefficient in Eq. (2) |
| $\theta_m$ | Azimuth angle of each wave component |
| $\varphi_{mn}$ | Initial phase angle of each wave component |
| $\rho_w$ | Density of water |
| $\eta$ | Free water surface elevation |
| $\xi_1$ | Coefficient in Eq. (10) |
| $\xi_2$ | Coefficient in Eq. (11) |
| $\delta$ | Correction parameter of the wave generator |

## References

Barclay, V.J., Bonner, R.F., Hamilton, I.P., 1997. Application of wavelet transforms to experimental spectra: smoothing, denoising, and data set compression. Anal. Chem. 69, 78–90.

Benjamin, T.B., Feir, J.E., 1967. The disintegration of wave trains on deep water. Part 1. Theory. *J. Fluid Mech.* 27, 417–430.

Bertin, X., de Bakker, A., van Dongeren, A., Coco, G., André, G., et al., 2018. Infragravity waves: from driving mechanisms to impacts. Earth Sci. Rev. 177, 774–799.

Biot, M.A., 1941. General theory of three-dimensional consolidation. J. Appl. Phys. 12, 155–164.

Biot, M.A., 1955. Theory of elasticity and consolidation for a porous anisotropic solid. J. Appl. Phys. 26 (2), 182–185.

Booij, N., Ris, R.C., Holthuijsen, L.H., 1999. A third-generation wave model for coastal regions 1. Model description and validation. J. Geophys. Res. 104, 7649–7666.

Canard, M., Ducrozet, G., Bouscasse, B., 2022. Varying ocean wave statistics emerging from a single energy spectrum in an experimental wave tank. Ocean Eng. 246, 110375.

Cartwright, D.E., Longuet-Higgins, M.S., 1956. The statistical distribution of the maxima of random function. Proc. R. Soc. London, Ser. A. 237, 212–232.

Cooley, J.W., Jukey, T.W., 1965. An algorithm for the machine calculation of complex Fourier series. Math. Comput. 19, 297–301.

de Groot, M.B., Kudella, M., Meijers, P., Oumeraci, H., 2006. Liquefaction phenomena underneath marine gravity structures subjected to wave loads. J. Waterw. Port, Coast. Ocean Eng. 132, 325–335.

Diaz, J., 2016. On the origin of the signals observed across the seismic spectrum. Earth Sci. Rev. 161, 224–232.

Gao, F.P., Li, J.H., Qi, W.G., Hu, C., 2015. On the instability of offshore foundations: theory and mechanism. Sci. China Phys. Mech. Astron. 58 (12), 124701.

Goda, Y., 1970. Numerical experiments on wave statistics with spectral simulation. Rep. Port Harbor Res. Inst. Jpn. 9, 3–57.

Goda, Y., 2000. Random Seas and Design of Maritime Structures. World Scientific Press, Singapore.

Goullet, A., Choi, W., 2011. A numerical and experimental study on the nonlinear evolution of long-crested irregular waves. Phys. Fluids 23 (1), 016601.

Hasselmann, D.E., Dunckel, L., Ewing, J.A., 1980. Directional wave spectra observed during JONSWAP 1973. J. Phys. Oceanogr. 10 (8), 1264–1280.

Hasselmann, K., 1962. On the non-linear energy transfer in a gravity-wave spectrum. Part 1. General theory. *J. Fluid Mech.* 12, 481–500.

Hasselmann, K., et al., 1973. Measurements of Wind-Wave Growth and Swell Decay during the Joint North Sea Wave Project (JONSWAP). *Ergnzungsheft zur Deutschen Hydrographischen Zeitschrift,* Reihe A (8°). Nr.12.

Herbers, T.H.C., Elgar, S., Guza, R.T., 1994. Infragravity-frequency (0.005-0.05 Hz) motions on the shelf. Part 1: forced waves. J. Phys. Oceanogr. 24, 917–927.

Hsieh, C.C., 2001. B-spline wavelet-based motion smoothing. Comput. Ind. Eng. 41, 59–76.

Hsu, J.R.C., Jeng, D.S., 1994. Wave-induced soil response in an unsaturated anisotropic seabed of finite thickness. Int. J. Numer. Anal. Methods GeoMech. 18 (11), 785–807.

Jeng, D.S., 1997. Wave-induced seabed instability in front of a breakwater. Ocean Eng. 24 (10), 887–917.

Jeng, D.S., 2001. Mechanism of the wave-induced seabed instability in the vicinity of a breakwater: a review. Ocean Eng. 28 (5), 537–570.

Jeng, D.S., 2013. Porous Models for Wave-Seabed Interactions. Shanghai Jiao Tong University Press, Shanghai (and Springer Press, Berlin).

Karshenas, A.M., Dunnigan, A.W., Williams, B.W., 1999. Wavelet power spectrum smoothing for random vibration control. IEEE Trans. Ind. Electron. 46 (2), 466–467.

Khintchine, A., 1934. Korrelationstheorie der stationaren stochastichen Prozesse. Math. Ann. 109, 604–615.

Klopman, G., van der Meer, J.W., 1999. Random wave measurements in front of reflective structures. J. Waterw. Port, Coast. Ocean Eng. 125 (1), 39–45.

Kumar, V.S., Kumar, K.A., 2008. Spectral characteristics of high shallow water waves. Ocean Eng. 35 (8–9), 900–911.

Lake, B.M., Yuen, H.C., 1978. A new model for nonlinear wind waves. Part 1. Physical model and experimental evidence. J. Fluid Mech. 88 (1), 33–62.

Li, C.F., Gao, F.P., 2022. Characterization of spatio-temporal distributions of wave-induced pore pressure in a non-cohesive seabed: amplitude-attenuation and phase-lag. Ocean Eng. 253, 111315.

Li, X.J., Gao, F.P., Yang, B., Zang, J., 2011. Wave-induced pore pressure responses and soil liquefaction around pile foundation. Int. J. Offshore Polar Eng. 21 (3), 233–239.

Liu, G., Yu, Y., Kou, Y., Du, X., Han, X., Wu, F., Liu, S., 2020. Joint probability analysis of marine environmental elements. Ocean Eng. 215, 107879.

Liu, H., Jeng, D.S., 2007. A semi-analytical solution for random wave-induced soil response and seabed liquefaction in marine sediments. Ocean Eng. 34, 1211–1224.

Longuet-Higgins, M.S., 1975. On the joint distribution of the periods and amplitudes of sea waves. J. Geophys. Res. 80 (18), 2688–2694.

Longuet-Higgins, M.S., Stewart, R.W., 1962. Radiation stress and mass transport in gravity waves, with application to 'surf beats. J. Fluid Mech. 13, 481–504.

Madsen, O.S., 1978. Wave-induced pore pressures and effective stresses in a porous bed. Geotechnique 87 (1), 377–393.

Miles, J.W., 1957. On the generation of surface waves by shear flows. J. Fluid Mech. 3, 185–204.

Miles, J.W., 1959. On the generation of surface waves by shear flows. Part 2. J. Fluid Mech. 6, 568–582.

Mitsuyasu, H., 1977. Measurement of the high-frequency spectrum of ocean surface waves. J. Phys. Oceanogr. 7 (6), 882–891.

Miyamoto, J., Sassa, S., Tsurugasaki, K., Sumida, H., 2020. Wave-induced liquefaction and floatation of a pipeline in a drum centrifuge. J. Waterw. Port, Coast. Ocean Eng. 146 (2), 04019039.

Moskowitz, L., 1964. Estimates of the power spectrums for fully developed seas for wind speeds of 20 to 40 knots. J. Geophys. Res. 69 (24), 5161–5179.

Niu, J., Xu, J., Dong, P., Li, G., 2019. Pore water pressure responses in silty sediment bed under random wave action. Sci. Rep. 9, 11685.

Phillips, O.M., 1957. On the generation of waves by turbulent wind. J. Fluid Mech. 2, 417–445.

Phillips, O.M., 1960. On the dynamics of unsteady gravity waves of finite amplitude. Part 1. The elementary interactions. J. Fluid Mech. 9, 193–217.

Pierson, W.J., Moskowitz, L., 1964. A proposed spectral form for fully developed wind seas based on the similarity theory of S. A. Kitaigorodski. *J. Geophys. Res.* 69 (24), 5181–5190.

Prasada Ran, C.V.K., 1988. Spectral width parameter for wind-generated ocean waves. Proc. Indian Acad. Sci. 97 (2), 173–181.

Qi, W.G., Gao, F.P., 2018. Wave induced instantaneously-liquefied soil depth in a non-cohesive seabed. Ocean Eng. 153, 412–423.

Qi, W.G., Shi, Y.M., Gao, F.P., 2020. Uplift soil resistance to a shallowly-buried pipeline in the sandy seabed under waves: poro-elastoplastic modeling. Appl. Ocean Res. 95, 102024.

Rahman, M.S., Layas, F.M., 1986. Pore pressure in ocean-floor sands under random waves. Mar. Georesour. Geotechnol. 6 (4), 341–358.

Ramamonjiarisoa, A., Mollo-Christensen, E., 1979. Modulation characteristics of sea surface waves. J. Geophys. Res. 84 (C12), 7769–7775.

Rueda-Bayona, J.G., Guzman, A., Eras, J.J.C., 2020. Selection of JONSWAPspectra parameters during water-depth and sea-state transitions. J. Waterw. Port, Coast. Ocean Eng. 146 (6), 04020038.

Ruiz, S., Saragoni, G.R., 2009. Free vibrations of soils during large earthquakes. Soil Dynam. Earthq. Eng. 29 (1), 1–16.

Sakai, T., Hatanaka, K., Mase, H., 1992. Wave-induced effective stress in seabed and its momentary liquefaction. J. Waterw. Port, Coast. Ocean Eng. 118 (2), 202–206.

Schäffer, H.A., 1996. Second-order wavemaker theory for irregular waves. Ocean Eng. 23 (1), 47–88.

Shemer, L., Singh, S.K., Chernyshova, A., 2020. Spatial evolution of young wind waves: numerical modelling verified by experiments. J. Fluid Mech. 901, A22.

Stewart, R.H., 2006. Introduction to Physical Oceanography. Press of Florida University, Florida.

Sui, T.T., Zhang, C., Jeng, D.S., Guo, Y.K., Zheng, J.H., Zhang, W., Shi, J., 2019. Wave-induced seabed residual response and liquefaction around a mono-pile foundation with various embedded depth. Ocean Eng. 173, 157–173.

Sumer, B.M., Fredsøe, J., Christensen, S., Lind, M.T., 1999. Sinking/floatation of pipelines and other objects in liquefied soil under waves. Coast. Eng. 38, 53–90.

Thomson, W.T., Dahleh, M.D., 2005. Theory of Vibration with Applications, fifth ed. Tsinghua University Press, Beijing.

Tucker, M.J., 1963. Analysis of records of sea waves. Proc. Inst. Cir. Eng. 26, 305–316.

Ulker, M.B.C., Rahman, M.S., Guddati, M.N., 2010. Wave-induced dynamic response and instability of seabed around caisson breakwater. Ocean Eng. 37 (17–18), 1522–1545.

Verruijt, A., 1969. Elastic storage of aquifers. In: Flow through Porous Media. Academic Press, New York, pp. 331–376.

Wang, J.X., Tang, X.B., 2010. Wavelet denoise method applied in load spectrum analysis of engineering vehicles. Adv. Mater. Res. 108–111, 1320–1325.

Wiener, N., 1930. Generalized harmonic analysis. Acta Math. 55, 117.

Xu, H., Dong, P., 2011. A probabilistic analysis of random wave-induced liquefaction. Ocean Eng. 38 (7), 860–867.

Yamamoto, T., Koning, H.L., Sellmeijer, H., Hijum, E.V., 1978. On the response of a poro-elastic bed to water waves. J. Fluid Mech. 87 (1), 193–206.

Zakharov, V.E., L'vov, V.S., Falkovich, G., 2012. Kolmogorov Spectra of Turbulence I: Wave Turbulence. Springer Science & Business Media, New York.